Geometric principles of second messenger dynamics in dendritic spines

Andrea Cugno[1], Thomas M. Bartol[2], Terrence J. Sejnowski[2,3], Ravi Iyengar[4], and Padmini Rangamani*[1]

[1]Department of Mechanical and Aerospace Engineering, University of California San Diego, CA, USA
[2]Howard Hughes Medical Institute, Salk Institute for Biological Studies, La Jolla, CA, USA
[3]Division of Biological Sciences, University of California, San Diego, San Diego, CA, USA
[4]Department of Pharmacological Sciences and Systems Biology Center New York, Icahn School of Medicine at Mount Sinai, New York, NY, USA

October 20, 2018

Abstract

Dendritic spines are small, bulbous protrusions along dendrites in neurons and play a critical role in synaptic transmission. Dendritic spines come in a variety of shapes that depend on their developmental state. Additionally, roughly 14∼19% of mature spines have a specialized endoplasmic reticulum called the spine apparatus. How do the shape of a postsynaptic spine and its internal organization affect the spatio-temporal dynamics of short timescale signaling? This question is central for understanding the beginnings of synaptic transmission, learning, and memory formation. In this work, we used mathematical modeling using reaction-diffusion equations in idealized geometries (ellipsoids and spheres) to characterize the effect of spine and spine apparatus geometries on the spatio-temporal dynamics of second messengers. Our analyses and simulations showed that in the short timescale, spine size and shape coupled with the spine apparatus geometries govern the spatiotemporal chemical dynamics of second messengers. We showed that the curvature of the geometries gives rise to *pseudoharmonic* functions, which predict the locations of maximum and minimum concentrations. Furthermore, we showed that the lifetime of the chemical gradient can be fine-tuned by localization of fluxes on the spine head and varying the relative curvatures and distances between the spine apparatus and the spine head. Thus, we identified several key geometric determinants of how spine head and spine apparatus may regulate the short timescale chemical dynamics of small molecules that control synaptic plasticity.

1 Introduction

Cell size, shape, and organelle location tightly regulate the dynamics of biochemical signal transduction; indeed even small molecule second messengers such as calcium (Ca^{2+}), cyclic adenosine monophosphate (cAMP), and inositol trisphosphate (IP_3) are reported to have distinct spatial microdomains within cells [1, 2]. Despite increasing observations about the localization of these signaling molecules, the role of cell size and shape in controlling local intracellular signaling reactions, and how this spatial information originates and is propagated remains poorly understood. It has been hypothesized that spatial and temporal separation of

*prangamani@ucsd.edu

second messengers can be a powerful means of specifying signaling functions through interplay of cell shape and biochemical regulators [3, 4]. Therefore, an emerging concept in the understanding of signal transduction is that cell signaling is profoundly inhomogeneous in space, and that the spatio-temporal dynamics of signal molecule activities create a code that confers signaling specificity [5, 6]. This concept has been approached both theoretically [4, 7, 8] and experimentally [9–11].

One particular cell type where shape and signaling are closely related is the neuron. Communication in neurons is mediated by synapses and consists in a complex cascade of signal transduction where the presynaptic terminals release neurotransmitters that are taken up by the post-synaptic spines to initiate a series of electrical, chemical, and mechanical events. Many of these events are tightly coupled by the dynamics of Ca^{2+}, $cAMP$, and IP_3 [12–14]. These second messengers are involved not only in the propagation of action potentials but also in downstream effects such as long-term potentiation (LTP), long-term depression (LTD), and structural plasticity. In particular, dendritic spines, which are thin post-synaptic protrusions, [15–17], have received much attention, especially because their density and morphology play a crucial role in mediating synaptic plasticity [18–22]. Changes in dendritic spine shape and density are symptomatic of several neuropathologies and neurodegenerative diseases such as Alzheimer's, Parkinson's, and drug addiction [23–27]. Thus, it is believed that the morphology of spines is closely related to their function: *de facto* reciprocal changes between the structure and function of spines impact both local and global integration of signals within dendrites [20, 28–30]. Recently, Ramirez et al. [31] proposed that a combination of the peculiar geometry of dendritic spines and a characteristic propagation of Cdc42 induce its localization longer than the one expected from the diffusion timescale alone.

Dendritic spines are characterized by characteristic shapes and internal organization. The mushroom-like morphology of mature spine is shown in Figure 1. A very thin ($40 \sim 100$ nm in diameter and $0.08 \sim 1.1$ μm long) neck separates the very viscous and rich in actin filaments bulbous head ($300 \sim 800$ nm in diameter) from the dendrite, suggesting that the spine head acts as an isolated signaling compartment [6, 32–34]. Additionally, roughly, the 14∼19% of spines contain a distinct organelle called the spine apparatus, which is a protrusion of the smooth endoplasmic reticulum (ER). The spine apparatus may also be of various shapes and sizes [6, 35–37]. It is generally accepted that changes in dendritic spine calcium levels, as well as local protein synthesis, play a central role in structural plasticity, and these two processes may be influenced by the presence and shape of a spine apparatus. Experimental observations have shown that mice lacking spine apparatus (synaptopodin-deficient mice) show deficits in LTP and impaired spatial learning, thus supporting the hypothesis that the spine apparatus is involved in synaptic plasticity [38–44]. Furthermore, it has been hypothesized that computational modeling of the spine could help to identify the regulatory feedback that govern the switch between LTD and LTP in ER-containing spines [45].

Despite the emerging importance of the role of spine shape and internal organization in synaptic plasticity, exactly how the physical aspects of a dendritic spine affect signaling dynamics of second messengers such as IP_3, Ca^{2+}, and cAMP remains poorly understood. In this paper, we conducted a systems biophysics study with the goal of identifying the design principles associated with the regulation of second messenger dynamics in dendritic spines. Specifically, using a combination of theory and computation, we sought to answer the following questions: (a) How are the spatio-temporal dynamics of second messengers within the spine affected by spine geometry? (b) How do the presence, size, and shape of the spine apparatus affect these spatio-temporal dynamics? And (c) how does different localization of the postsynaptic density (PSD, a protein-dense region in the postsynaptic membrane) affect the spatio-temporal dynamics of the second messenger? We showed that in the short timescale, the geometric features of the spine play an important role in establishing the spatio-temporal dynamics of the second messengers.

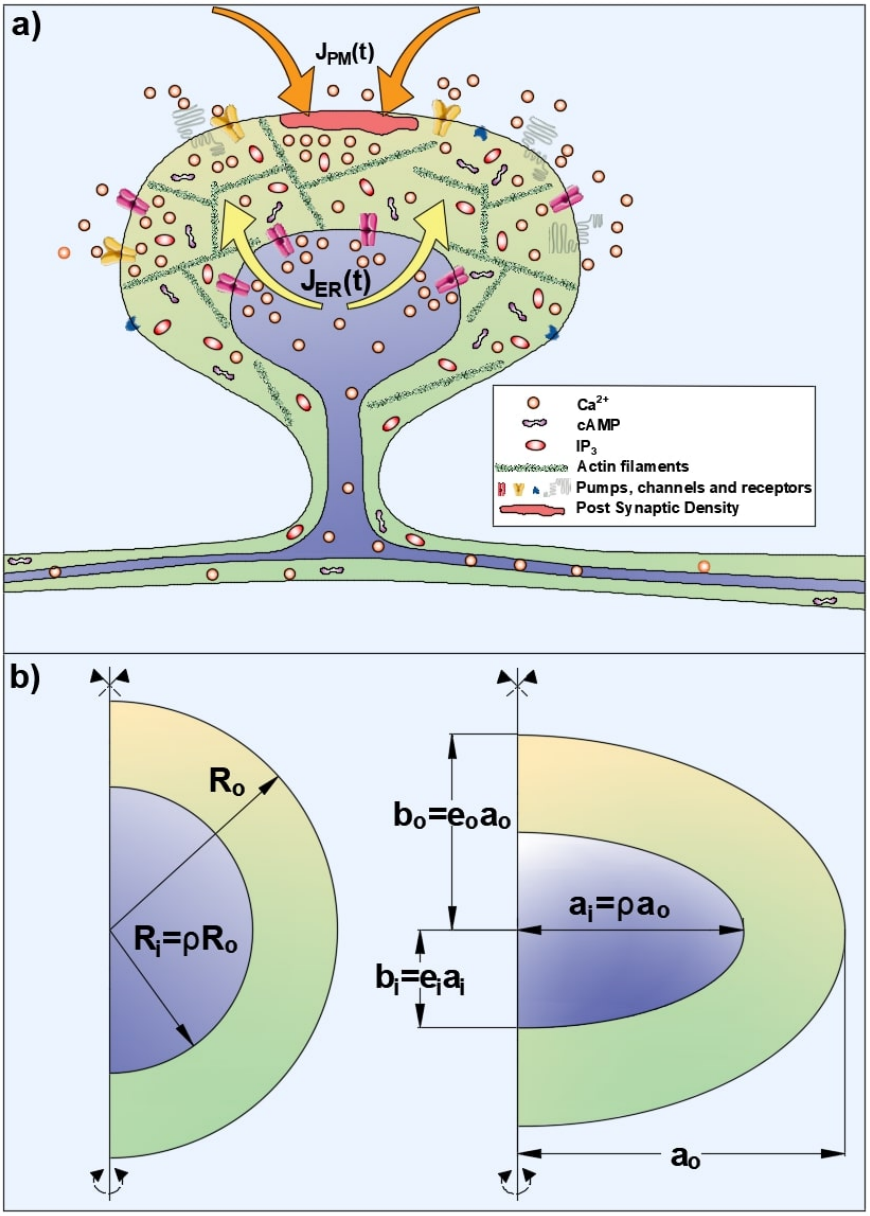

Figure 1: a) Schematic of a typical dendritic spine. Pumps, channels, and receptors on the plasma membrane (PM) and on the endoplasmic reticulum (ER) membrane allow for fluxes of second messengers such as Ca^{2+}, IP_3, and cAMP. These fluxes can be modeled as time-dependent flux boundary conditions – $J_{PM}(t)$ at the plasma membrane and $J_{ER}(t)$ on the inner membrane. In addition to reaction-diffusion dynamics in the domain, these fluxes determine the spatio-temporal dynamics of second messenger concentration in signaling subcompartments such as dendritic spines. b) Geometries used to simulate the different spine shapes: spherical shell with outer radius R_o and inner radius $R_i = \rho R_o$; oblate spheroidal shell with outer eccentricity e_o and inner eccentricity e_i. The dimensions of the outer shell are major axis a_o and minor axis $b_o = e_o a_o$ and the dimensions of the inner shell are major axis $a_i = \rho a_o$ and minor axis $b_i = e_i a_i$. For all simulations in this study, we define the outer radius (and major axis) as $R_o = a_o = 250\ nm$.

2 Methods

2.1 Governing equations

We developed and analyzed a reaction-diffusion model of second messenger dynamics with time-dependent flux boundary conditions. The resulting system of equations was analytically and numerically solved in simplified geometries to identify how the dynamics of second messengers are related to the geometrical parameters (see Figure 1b). We considered a second messenger with concentration distribution $C = C(\mathbf{x}, t)$, where $\mathbf{x}$ is a vector defining the spatial coordinates and t is time. In the volume of the domain, the dynamics of C are then given by the following partial differential equation (PDE):

$$\frac{\partial C}{\partial t} + \frac{1}{\tau} C = D \nabla^2 C, \tag{1}$$

where D is the diffusion constant of the species C, ∇^2 represents the Laplacian operator in three dimensions, and τ is a time constant representing the consumption or decay of C; we used $\tau = 50\ ms$ for all simulations, to be consistent with experimental [46] or simulation data [6] .

2.2 Boundary conditions

To completely define the dynamics of C in the domain, we needed to prescribe boundary conditions on both the PM and ER membrane. Since the dynamics of the receptor-mediated events at the PM and on the organelle membranes are time-dependent fluxes due to signaling molecules [47–50], we prescribed the following boundary conditions:

$$\nabla C \cdot \hat{\mathbf{n}}|_{PM} = J_{PM}(t), \quad \nabla C \cdot \hat{\mathbf{n}}|_{ER} = J_{ER}(t), \tag{2}$$

where the fluxes J_{PM} and J_{ER} depend on many nonlinear reaction kinetic terms. For the purposes of our analyses, we used biexponential functions to describe the PM flux and included a slight delay in the ER flux to result in

$$J_{PM}(t) = \delta \left(e^{-\frac{t}{\alpha}} - e^{-\frac{t}{\beta}} \right) \quad \text{and} \quad J_{ER}(t) = \eta\ J_{PM}(t - t_{ER}), \tag{3}$$

where the amplitude parameter δ, the time constants α and β, the amplitude PM-ER flux ratio η as well as the ER delay t_{ER} are free parameters that can be fit to experimental [46] or simulation data [6].

2.3 Geometries

We modeled the volume between the plasma and ER membrane of the dendritic spine head using idealized geometries such that, to first approximation, they resemble the shape of a mature spine. We used two idealized geometries, a spherical and an oblate spheroidal shells (see Figure 1b). The dimensions of the spherical shell shape are denoted as outer radius R_o and internal $R_i = \rho R_o$. To highlight the combined effect of curvatures and size of the membranes, we considered oblate spheroidal shells with outer eccentricity e_o and inner eccentricity e_i. As a result, the dimensions of the outer shell are major axis a_o and minor axis $b_o = e_o a_o$ and the dimensions of the inner shell are major axis $a_i = \rho a_o$ and minor axis $b_i = e_i a_i$. In this study, the geometrical parameters ρ, e_i, and e_o have been varied (in the range (0, 1]) to quantify the geometrical influence on the spatio-temporal dynamic of second messengers (C). For all simulations, we considered the outer radius (and major axis) as $R_o = a_o = 250\ nm$. (see Figure 1b).

2.4 Computational tools

To assist in the derivation of the analytical solutions (Section 3.1) we used Mathematica 11.3 [51]. Simulations for the dynamics of second messenger were performed using finite element methods available through the commercial package COMSOL Multphysics 5.3a with MATLAB2018a [52]. In particular, the coefficient form PDE interface was used considering parametrized geometries and the solutions were produced with the parametric sweeps utility. Wolfram Mathematica 11.3 and MATLAB2018a [53] were used for post-processing the solution and making the figures.

2.5 Model analysis and relevant parameters

To compare the effect of different model geometries on the spatiotemporal dynamics of C, we defined the following metrics:

Gradient Metric: In order to quantify a local measure of the spatial gradient of the species C, we used

$$||\nabla C|| = \sqrt{\left(\frac{\partial C}{\partial x_i}\mathbf{e}_i\right) \cdot \left(\frac{\partial C}{\partial x_i}\mathbf{e}_i\right)} \tag{4}$$

where x_i are the components of the position vector $\mathbf{x}$ in the direction defined by the vector bases $\mathbf{e}_i$, $i = \{1, 2, 3\}$, and the Einstein notation of repeated indices was used.

Extent of variability: A global measure of the variability of second messenger in the spine was defined as:

$$\Psi(t) = \frac{C_{max} - C_{min}}{C_{mean}} \tag{5}$$

where C_{max}, C_{min}, and C_{mean} are the maximum, minimum, and spatially averaged value of concentration of C in the spine respectively. This quantity gives us insight on the localization of second messengers. When $\Psi(t)$ is equal to zero, there is no concentration gradient in the spine.

Lifetime of localization: Defined as the time needed to let $\Psi(t)$ be lower than a threshold value Ψ_{th}. In this work, we used $\Psi_{th} = 25\%$ as the value beyond which the distribution of C is uniform.

$$\tau_\Psi = t^* : \quad \Psi(t^*) < \Psi_{th} \tag{6}$$

For the sake of clarity, the parameters used in the model are summarized in Table 1.

3 Results

3.1 Analytical solution

Eq. (1) is a *homogeneous* PDE with time-dependent BCs given by Eq. (2). To solve it, we used the method of the *Generalized eigenfunction expansion* after formally transforming the problem into one with homogeneous boundary conditions, as a result the PDE becomes nonhomogeneous [54]. We defined a function, the so-called *reference concentration distribution* $w(\mathbf{x}, t)$, such that it satisfies the given nonhomogeneous boundary condition, *i.e.*:

$$\nabla w \cdot \hat{\mathbf{n}}|_{PM} = J_{PM}(t) \ , \quad \nabla w \cdot \hat{\mathbf{n}}|_{ER} = J_{ER}(t) \tag{7}$$

We considered a solution for C such that

$$C = v + w, \tag{8}$$

Table 1: Notation used in the model

Symbol	Description	Units
C	Concentration of second messenger	μM
D	Diffusion constant of C	$\mu m^2/s$
τ	Decay time constant	ms
$J_{PM}(t)$	Time-dependent flux at the plasma membrane	$\mu M \cdot \mu m/ms$
$J_{ER}(t)$	Time-dependent flux at the endoplasmic reticulum membrane	$\mu M \cdot \mu m/ms$
δ	Amplitude parameter for the PM flux	$\mu M \cdot \mu m/ms$
α, β	Flux time constants	ms
η	ER/PM amplitude ratio	-
t_{ER}	ER time delay	ms
R_o	Radius of the outer spherical boundary	nm
R_i	Radius of the inner spherical boundary	nm
a_o and b_o	Major and minor axes of the outer oblate spheroidal boundary	nm
a_i and b_i	Major and minor axes of the inner oblate spheroidal boundary	nm
$\rho = \frac{R_i}{R_o}$ (or $= \frac{a_i}{a_o}$)	Ratio between the inner-outer radii (or major axes)	-
e_i	Inner eccentricity	-
e_o	Outer eccentricity	-
$\|\|\nabla C\|\|$	Metric of the spatial gradient of second messengers	$\mu M/\mu m$
$\Psi(t)$	Extent of variability	-
$\Psi_{th} = 25\%$	Threshold value for Ψ	-
τ_Ψ	Lifetime of localization	ms

where the unknown function v is the solution of the new nonhomogeneous PDE with homogeneous BCs obtained by substituting Eq. (8) into Eq. (1), resulting in:

$$\begin{aligned} PDE: &\quad \frac{\partial v}{\partial t} = D\nabla^2 v - \frac{1}{\tau} v + Q, \\ BCs: &\quad \nabla v \cdot \hat{\mathbf{n}}|_{PM} = 0, \quad \nabla v \cdot \hat{\mathbf{n}}|_{ER} = 0 \end{aligned} \tag{9}$$

where $Q = D\nabla^2 w - \frac{\partial w}{\partial t} - \frac{1}{\tau} w$ is a source term for v. For a homogeneous initial condition for C, the following initial condition holds for v and w:

$$v|_{t=0} = -w|_{t=0} = g(\mathbf{x}). \tag{10}$$

To solve Eq. (9) the method of *eigenfunction expansion* is used, which consists of expanding the unknown function v in a series of *spatial* eigenfunctions Λ:

$$v(\mathbf{x}, t) = \sum_{n=1}^{\infty} T_n(t) \Lambda_n(\mathbf{x}). \tag{11}$$

Here, $T_n(t)$ are the generalized Fourier coefficients of the eigenfunctions $\Lambda_n(\mathbf{x})$. From here on, the Einstein notation for repeated indices will be used. The eigenfunctions are the solution of the *associated* homogeneous version ($Q = 0$) of Eq. (9). Using the method of separation of variables, $v = T(t)\Lambda(\mathbf{x})$, we can write:

$$\frac{1}{T}\frac{dT}{dt} = -\left(\lambda^2 + \frac{1}{\tau}\right), \text{ and} \tag{12}$$

$$\frac{\nabla^2 \Lambda}{\Lambda} = \frac{-\lambda^2}{D}, \tag{13}$$

where λ is a separation constant.

The separation between time and space highlights the *pseudo-harmonic* nature of the distribution of second messenger (C). The time ordinary differential equation (ODE in Eq. (12)) has an exponential decay as the solution, which is affected by both λ and the consumption rate τ. The spatial PDE in Eq. (13) represents the Helmholtz wave equation, which is separable in 11 three-dimensional coordinate systems, and for each of them, there exists a specific family solutions, called the harmonic wave functions [55, 56]. However, the presence of internal and external time-dependent boundary conditions and the transcendental nature of the kernel of the solution limit the possibility of finding explicit solutions, restricting the solution to an *implicit form*. In Sections 3.1.1 and 3.1.2, we further specialize this analysis for spherical and oblate spheroidal shells.

3.1.1 Analysis in spherical shells

In the case of spherical shell domain with inner boundary with radius R_i and outer radius R_o, we considered a spherical coordinate system ($\mathbf{x} = (r\,\mathbf{e_r},\ \theta\,\mathbf{e}_\theta,\ \phi\,\mathbf{e}_\phi)$) defined in term of the Cartesian (x, y, z) coordinates as showed in Figure 2, where $r \in [R_i, R_o]$, $\theta \in [0, 2\pi)$, and $\phi \in [0, \pi]$ represent the radial, the azimuth,

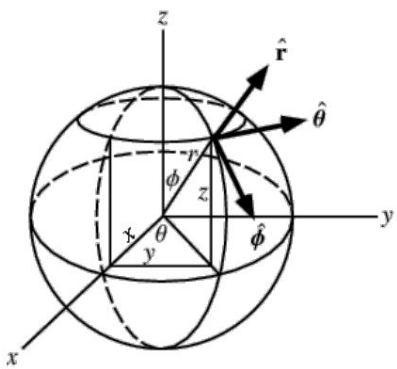

$$x = r\cos\theta\sin\phi \qquad r \in [R_i, R_o]$$
$$y = r\sin\theta\sin\phi \qquad \theta \in [0, 2\pi)$$
$$z = r\cos\phi \qquad \phi \in [0, \pi]$$

Figure 2: Spherical coordinate system [57].

and zenith coordinates respectively [57]. Exploiting the spherical symmetry of both the domain and the boundary condition, we assume the $C(\mathbf{x}, t)$, and thus $v(\mathbf{x}, t)$, and $w(\mathbf{x}, t)$, spatially depend just on the radial coordinate r, and there is no dependence on the angular coordinates θ and ϕ. Thus, the Laplace and normal gradient operators are:

$$\nabla^2 = \frac{1}{r}\frac{\partial}{\partial r}\left(r\frac{\partial}{\partial r}\right) \quad \text{and} \quad \nabla\cdot\hat{\mathbf{n}} = \frac{\partial}{\partial r}\hat{\mathbf{r}}. \tag{14}$$

In this framework the simplest way to define $w(r, t)$ respecting the conditions in Eq. (7) is

$$w(r,t) = J_{ER}(t)(r - R_i) - (J_{PM}(t) + J_{ER}(t))\,\frac{(r - R_i)^2}{2\,(R_o - R_i)}. \tag{15}$$

Considering the homogeneous initial condition for C and Eq. (15) the initial condition for v is:

$$v(r,0) = -J_{ER}(0)(r - R_i) + (J_{PM}(0) + J_{ER}(0))\,\frac{(r - R_i)^2}{2\,(R_o - R_i)} = g(r). \tag{16}$$

The solution of Eq. (13) in spherical coordinates is the sum of spherical Bessel functions of the first (J) and the second (Y) kind of zero order [54–56], *i.e.*:

$$\Lambda(r) = a\ J(\lambda r) +\ b\ Y(\lambda r), \tag{17}$$

where a and b are integration constants.

Due to the homogeneity of both PDE and BCs, there exists a non-trivial solution for v if we impose the *determinant condition* [54]. The BCs in Eq. (9) now become:

$$\begin{aligned} \left(a\frac{\partial J(\lambda r)}{\partial r} + b\frac{\partial Y(\lambda r)}{\partial r}\right)\Big|_{r=R_i} &= 0, \\ \left(a\frac{\partial J(\lambda r)}{\partial r} + b\frac{\partial Y(\lambda r)}{\partial r}\right)\Big|_{r=R_o} &= 0. \end{aligned} \tag{18}$$

The eigenvalues λ_n are the roots of the *characteristic polynomial*:

$$p(\lambda) = \frac{\partial J(\lambda r)}{\partial r}\Big|_{r=R_i}\frac{\partial Y(\lambda r)}{\partial r}\Big|_{r=R_o} - \frac{\partial J(\lambda r)}{\partial r}\Big|_{r=R_o}\frac{\partial Y(\lambda r)}{\partial r}\Big|_{r=R_i} \tag{19}$$

After some manipulation, and exploiting the properties of the Bessel functions, it is possible to rearrange $p(\lambda)$ as follows:

$$p(\lambda_D) = \left(\lambda_D^2\rho + 1\right)\sin\left(\lambda_D(1-\rho)\right) + \lambda_D(\rho - 1)\cos\left(\lambda_D(1-\rho)\right), \tag{20}$$

where $\lambda_D = \frac{\lambda R_o}{\sqrt{D}}$ and $\rho = \frac{R_i}{R_o}$.

As shown in Eq. (20), $p(\lambda_D)$ is a transcendental function and the zeros can be found only numerically as showing in Figure 3.

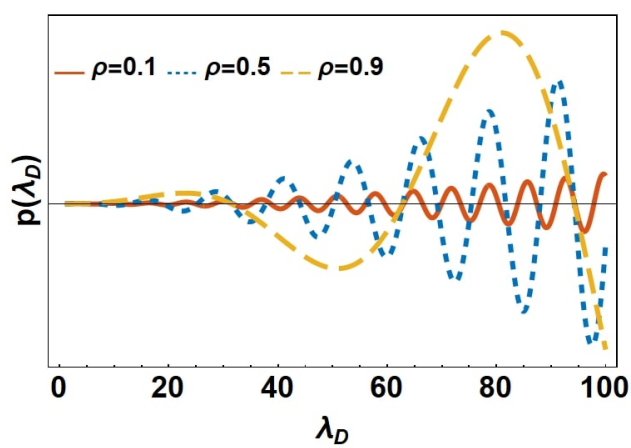

Figure 3: Function $p(\lambda_d)$ for different values of the ratio ρ. All the zero-crossing represent the eigenvalues λ_n of Eq. (13).

Assuming that the eigenvalues λ_n have been found, the expansion in Eq. (11) can thus be specialized as follows:

$$v(r,t) = a_n(t)J(\lambda_n r) + b_n(t)Y(\lambda_n r). \tag{21}$$

Exploiting the orthogonality of the eigenfunctions we can now determine the initial values of the generalized Fourier coefficients as follows [54]:

$$a_n(0) = \frac{\int_{R_i}^{R_o} g(r)J(r)\ dr}{\int_{R_i}^{R_o} J(r)^2\ dr} \quad \text{and} \quad b_n(0) = \frac{\int_{R_i}^{R_o} g(r)Y(r)\ dr}{\int_{R_i}^{R_o} Y(r)^2\ dr}\ . \tag{22}$$

Substituting Eq. (21) back into Eq. (9), due to the orthogonality of the eigenfunctions, one obtains the two nonhomogeneous first time ODEs for the Fourier coefficients that must respect the initial conditions in

Eq. (22):

$$\frac{da_n}{dt} + (\lambda_n^2 + \frac{1}{\tau})a_n = \frac{\int_{R_i}^{R_o} Q(r,t)J(r)\ dr}{\int_{R_i}^{R_o} J(r)^2\ dr} \equiv q_a(t), \quad \frac{db_n}{dt} + (\lambda_n + \frac{1}{\tau})b_n = \frac{\int_{R_i}^{R_o} Q(r,t)Y(r)\ dr}{\int_{R_i}^{R_o} Y(r)^2\ dr} \equiv q_b(t) \quad (23)$$

The solution of the previous equations leads to:

$$a_n(t) = a_n(0)e^{-(\lambda_n^2+\frac{1}{\tau})t} + e^{-(\lambda_n^2+\frac{1}{\tau})t}\int_0^t q_a(t)e^{(\lambda_n^2+\frac{1}{\tau})t}\ dt \quad (24)$$

$$b_n(t) = b_n(0)e^{-(\lambda_n^2+\frac{1}{\tau})t} + e^{-(\lambda_n^2+\frac{1}{\tau})t}\int_0^t q_b(t)e^{(\lambda_n^2+\frac{1}{\tau})t}\ dt. \quad (25)$$

Finally, it is worth highlighting how in Eqs. (24) and (25), the amplitude of the wave functions are implicitly related (through Q) to the spatio-temporal distribution of the biochemical reactions on the membranes of the spine, intricately coupled by the morphology (through λ_n) and reaction kinetics (through τ).

3.1.2 Analysis in oblate spheroidal shells

In the case of confocal oblate spheroidal shell (Figure 1b), with a_o and $b_o = e_o a_o$, the major and minor outer axes respectively, and $a_i = \rho a_o$ and $b_i = e_o a_i$ the inners ones, we used oblate spheroidal coordinates system $\mathbf{x} = (\xi\,\mathbf{e}_\xi,\ \eta\,\mathbf{e}_\eta, \phi\,\mathbf{e}_\phi)$ related to the Cartesian coordinates as shown in Figure 4. Surfaces $\xi = constant$, $\eta = constant$, and $\phi = constant$ are oblate spheroids, confocal one-sheeted hyperboloids of revolution, and planes through the z-axis respectively.

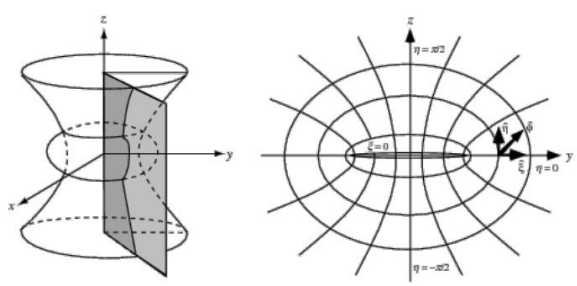

$$x = a_o\sqrt{(\xi^2+1)(1-\eta^2)}\cos\phi, \qquad \xi \in [a_i, a_o]$$
$$y = a_o\sqrt{(\xi^2+1)(1-\eta^2)}\sin\phi, \qquad \eta \in [-1, 1]$$
$$z = a_o\xi\eta, \qquad \xi \in [0, 2\pi]$$

Figure 4: Spheroidal coordinates system [58].

In this coordinate system the Laplacian operator can be expressed as follows ([55, 56, 58–61])

$$\nabla^2 = \frac{1}{a_o^2(\xi^2+\eta^2)}\left(\frac{\partial}{\partial\xi}\left((\xi^2+1)\frac{\partial}{\partial\xi}\right) + \frac{\partial}{\partial\eta}\left((1-\eta^2)\frac{\partial}{\partial\eta}\right) + \frac{\xi^2+\eta^2}{(\xi^2+1)(1-\eta^2)}\frac{\partial^2}{\partial\phi^2}\right). \quad (26)$$

The normal gradient to the boundary of oblate ellipsoids is defined as:

$$\nabla\cdot\hat{\mathbf{n}} = \frac{1+\xi^2}{a_o^2(\xi^2+\eta^2)}\frac{\partial}{\partial\xi}\mathbf{e}_\xi \quad (27)$$

We assume that it is possible to establish a reference function w such that it respects the BCs (Eq. (7)) specialized by means Eq. (27) in oblate spheroidal coordinates. In this framework, the Helmholtz equation in Eq. (13) admits solution in the form $\Lambda = w_1(\xi)w_2(\eta)w_3(\phi)$, where w_1, w_2, and w_3 satisfy the following

spheroidal wave equations respectively [55, 56, 59–61]:

$$\frac{\mathrm{d}}{\mathrm{d}\xi}\left((1+\xi^2)\frac{\mathrm{d}w_1}{\mathrm{d}\xi}\right)-\left(k+\gamma^2(1+\xi^2)-\frac{\mu^2}{1+\xi^2}\right)w_1=0, \tag{28}$$

$$\frac{\mathrm{d}}{\mathrm{d}\eta}\left((1-\eta^2)\frac{\mathrm{d}w_2}{\mathrm{d}\eta}\right)+\left(k+\gamma^2(1-\eta^2)-\frac{\mu^2}{1-\eta^2}\right)w_2=0, \tag{29}$$

$$\frac{\mathrm{d}^2w_3}{\mathrm{d}\phi^2}+\mu^2w_3=0. \tag{30}$$

with $\gamma^2=-\lambda^2a_o/D$ and, k and μ^2 are new separation constants. The solution of Eqs. (28)–(30) involve the *spheroidal harmonic functions*:

$$w_1(\xi)=a_1S_n^{\mu(1)}\left(i\xi,\gamma\right)+b_1S_n^{\mu(2)}\left(i\xi,\gamma\right), \tag{31}$$

$$w_2(\eta)=a_2P_n^{\mu}\left(\eta,\gamma^2\right)+b_2Q_n^{\mu}\left(\eta,\gamma^2\right), \tag{32}$$

$$w_3(\phi)=a_3\cos\left(\mu\phi\right)+b_3\sin\left(\mu\phi\right). \tag{33}$$

Here the eigenfunctions S, P and Q are the so-called *radial wave* functions, *spheroidal wave functions of first kind* and *spheroidal wave functions of second kind* respectively, while a_1, a_2, b_1, b_2, c_1, and c_2 are integration constants. The oblate spheroidal solution can be simplified assuming the oblate symmetry of both the geometry and the BCs and thus we assume that $\Lambda=w_1(\xi)w_2(\eta)$ and $\mu=0$. Also in this case, the eigenvalues can be found, imposing the determinant condition, in an implicit form. Similarly to the spherical case (Eqs. (24)–(25)) the generalized Fourier coefficients (Eq. (11)) will have an exponential time decay highlighting the pseudo-harmonic nature of the solution.

3.2 Combined effect of spine apparatus size and diffusion coefficient on the lifetime of second messenger gradient

We begin with an analysis of the spatiotemporal dynamics of C in a spherical spine head of radius $r=R_o$ and a spherical spine apparatus with a radius $R_i=\rho R_o$ (Figure 1 and Table 1). For illustrative purposes, we chose a set of parameters for the boundary conditions (Figure 5a) such that we can match previously reported dynamics of calcium [6]. For a diffusion coefficient $D=100\ \mu m^2/s$ and $\rho=0.5$, the profile of C at a location exactly halfway between the two membranes is shown in (red line, Figure 5b); this temporal profile is in good agreement with previous observations (see inset in Figure 5b). Therefore, for all the following simulations, we used the time constants (α, β, and t_{ER}) as shown in Figure 5a, but the amplitude parameters (γ and η) have been customized to the specific geometry, to avoid abnormal peaks of concentration of second messengers.

A characteristic feature of spatio-temporal dynamics of C is the lifetime of the gradient, which is affected by both the ratio between the radii (ρ) and the diffusion coefficient (D). To decode how these two quantities affect the spatiotemporal dynamics of C, we conducted the following simulations – (i) Spine apparatus size was varied by changing ρ; we used three different values of ρ (0.1, 0.5, and 0.9) to capture the extreme volume changes due to small, medium, and large spine apparatus. (ii) Diffusion constant of C was varied to capture the range of intracellular diffusion from a crowded regime to free diffusion (1, 10, 100 $\mu m^2/s$) [62–67]. We found that when the spine apparatus is small ($\rho=0.1$), an appreciable concentration variability exists in the radial direction when the diffusion coefficient is small ($D=1\mu m^2/s$) at early time points but not for larger diffusion coefficients (Figure 6a). As the spine apparatus gets larger, there is less volume available in the spine and more surface area for the internal membrane (more J_{ER}). Therefore, the variability of C is smaller even for a lower diffusion coefficient (Figure 6b,c).

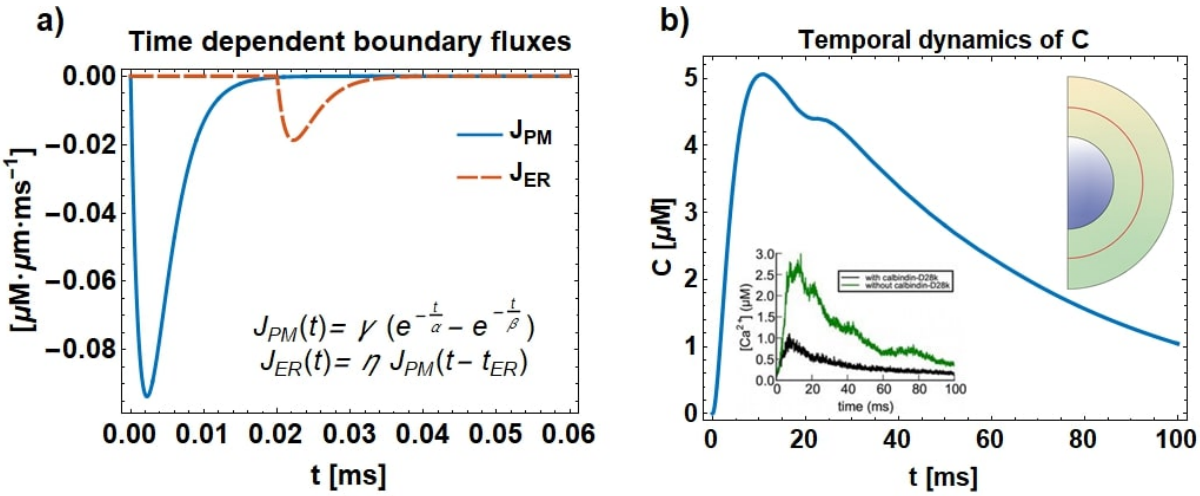

Figure 5: a) Time-dependent boundary fluxes for the outer membrane (solid blue) and inner membrane (dashed red) respectively, representing the dynamics of various pumps and channels; $D = 100\ \mu m^2/s$, and $\rho = 0.5$. The flux parameters ($\alpha = 2.5\ ms,\ \beta = 2\ ms,\ \gamma = -1.14\times10^{-6}\ \mu M\cdot\mu m/ms,\ \eta = 0.2,$ and $t_{ER} = 20\ ms$) have been fitted to reproduce typical temporal dynamics of second messengers inside a dendritic spine. b) Temporal dynamics of C, in μM, at the midpoint between the inner and outer shells ($r^* = (R_o - R_i)/2 + R_i$, red line). Inset shows the data MCell simulation from [6] for Ca^{2+} dynamics.

To quantify the lifetime of the gradient in these cases, we calculated the norm of the gradient of C as a function of time. Again, when the spine apparatus is small and the diffusion coefficient is small, the gradient lasts longer and an increase in diffusion coefficient for a given spine apparatus size reduces the lifetime (Figure 6d). As the size of the spine apparatus increases, even for small diffusion coefficients, the lifetime of the gradient decreases (Figure 6e, f) confirming that small apparatus and low diffusion will result in longer in time gradients of C, while a large apparatus, even with a small diffusion coefficient will result in rapid propagation of second messenger from the PM to the ER membrane. Therefore, one potential design principle that we have identified here is that despite the low diffusion of small molecules in crowded intracellular spaces [63–67] (see Appendix A for a detailed discussion), dendritic spines may be able to ensure rapid and robust signal propagation by increasing the size of the spine apparatus and thereby reducing the distance that signaling molecules need to travel before reacting with their effector molecules.

3.3 Size and shape of the spine and spine apparatus affects the gradient of signaling molecules

We next investigated the effect of the shape of the spine and the spine apparatus. This is particularly relevant since dendritic spines are known to have distinct shapes and their shape is associated with function [20, 28, 29]. Because shape of the spine is a result of many different geometric properties, we focused specifically on curvature by modeling the spine shapes as different ellipsoidal shells. Even though this is a mathematical idealization, the resulting solutions provide insight into how curvature variations along the ellipsoids affect the harmonic functions that govern the profile of C, for uniformly spatially distributed boundary conditions. As before, the size of the domain is controlled by ρ and now the shape is controlled by the eccentricities of the inner and outer ellipsoids e_i and e_o respectively (Figure 1 and Table 1). We conducted a systematic variation of the magnitude of these geometrical parameters and analyzed their effect on the spatio-temporal

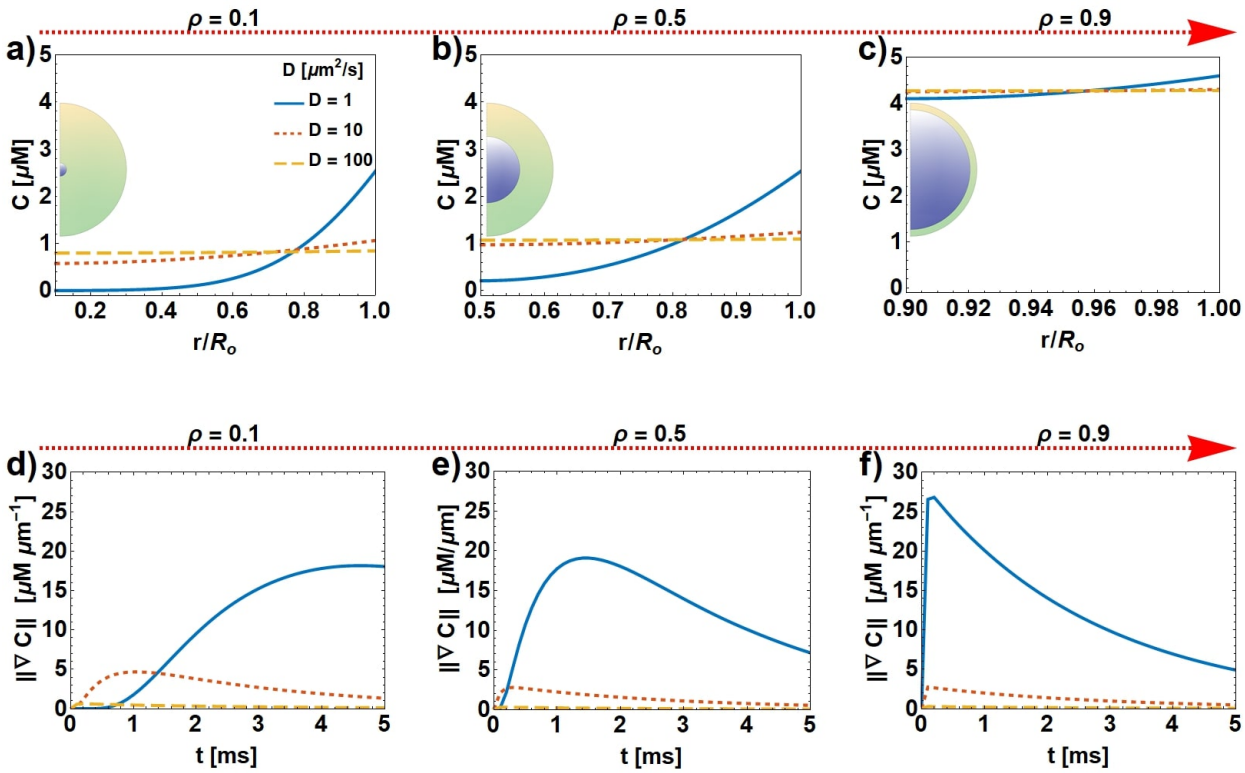

Figure 6: Effect of spine apparatus size and diffusion constant D on the lifetime of C: The top row shows the radial distribution of C concentration for three different values of diffusivities ($D = 1,\ 10,\ 100\ \mu m^2/s$) at 1 ms: a) $\rho = 0.1$, b) $\rho = 0.5$, and c) $\rho = 0.9$. The bottom row shows the norm of the concentration gradient ($||\nabla C||$), a local measure of the spatial variability, for d) $\rho = 0.1$, e) $\rho = 0.5$, and f) $\rho = 0.9$, respectively at the midpoint between the inner and outer shells ($r^* = (R_o - R_i)/2 + R_i$).

dynamics of C (Figure 7).

For a given value of e_o and e_i, both set to 0.5 in this case, as ρ increases, the location of maximum concentration changes from the equator to the pole. This is because of the *pseudoharmonic* nature of the solutions (Figure 7a) and a complex interplay among curvatures and distance between the membranes that induce a nonuniform distribution of the surface (and thus flux) per available volume: where the outer membrane is more curved there is more surface per volume and thus is where higher levels of concentration are reached. The increase of the flux per volume can also be caused by changing the distance between the membranes. In fact, when this distance is too small, the curvature effects became secondary. Furthermore, when there is less volume available in the spine (increasing ρ), the overall concentration of C increases. For a constant ρ and e_o, increasing e_i, which results in the spine apparatus tending towards a spherical geometry (Figure 7b), C passes from a spherical-like distribution ($e_i = 0.1$) to a localization of the maximum on the pole ($e_i = 1$) through an intermediate situation where the maximum is confined in the equator ($e_i = 0.5$). These results hold even in the case of constant ρ and e_i and decreasing e_o (Figure 7c). Thus, the shape and size effects of the spine and spine apparatus are a result of PM shape and ER membrane shape and the relative volume enclosed. In fact, a significant difference between maximum and minimum peaks hold for few milliseconds, before a well-mixed condition is reached (Figure 7d), as showed by the asymptotic evolution of Ψ (Figure 7e).

We plotted τ_Ψ (Table 1) as a function of ρ, e_i, and e_o (Figure 7f). Given the complexity of this space, we showed three specific smoothed surfaces (see Figure B.1 for the raw data) of constant e_o for purposes of clarity. If τ_Ψ were unaffected by geometric parameters, we would expect to see a flat plane for each value of e_o. However, we see that the τ_Ψ surface for each value of e_o has a valley where the lifetime is short and peaks at the extreme edges of ρ and e_i. When e_o increases, the valley becomes more shallow and the location of the minimum shifts. Thus, the lifetime of the gradient depends on the geometry of the inner and outer membranes in a highly nonlinear manner.

The results from these simulations can be summarized as follows: *first*, unlike spherical shells where the spatial variation is only in the radial direction, ellipsoidal shells show a spatial variation in the z and the r directions (Figure 7a-c); *second*, the spatial variation of C, particularly the location of high and low concentrations of C at a given time can switch from the equator to the pole or *vice versa* depending on the geometry alone (Figure 7a-c); *third*, the timescale τ_Ψ over which an appreciable gradient lasts is a complex nonlinear function of these geometric quantities due to both shape and BCs coupling (Figure 7d-f), varying quantitatively in the range [0.2∼4.2] ms and showing that there are regions of the spine subjected to transient differentiated level concentration (Figure 7d-f). Thus, these simulations predict that a deviation from spherical shape provides spines access to a more complex phase space with respect to the properties of the gradient of C and its lifetime.

3.4 Consequences of a localized input of second messenger in dendritic spine

Thus far, we have shown that geometry by itself, in the presence of homogeneous boundary conditions, produces transient localization of second messenger. However, in reality, these fluxes are not uniform but are localized to specific regions of the spine head. In fact, as shown by the reconstruction of many dendritic spines [6, 37, 68–71], the post-synaptic density, a portion of the PM rich in receptors, is localized along different positions of the membrane. Therefore, we next analyzed the combined effect of spine geometries and BCs localized to specific portions of the boundary.

We first considered a spine where the flux is confined in the upper pole region of the head. (Figure 8a-d)). In this representative case ($\rho = 0.9$, $e_o = 0.8$, and $e_i = 0.7$), there is a significant localization of high concentration of C close to the pole and this holds for more than 10 ms (Figure 8b-d)). The gradient extends from the top of the spine head to the bottom with the spine apparatus acting as a geometric barrier for diffusion of C. The lifetime of the localization also depends to the geometrical parameters, and the smoothed surfaces $\tau_\Psi(\rho, e_i, e_o)$ in Figure 8e (see Figure B.2 for the raw data) showed how, unlike the case with uniform BCs, the localization of influx dramatically increases the lifetime of localization (τ_Ψ up to 26 ms). Even though these surfaces continue to exhibit a nonlinear dependence on the geometric parameters, curvatures and spine apparatus size, for localized boundary conditions, the effect of ρ appears to be predominant.

These effects can also be seen if the localized BC at the PM is confined to a side of the spine as shown in Figure 8f. Similarly, to the localized pole BC, there is a significant localization of the maximum peak in the top part of the spine and a nonuniform concentration lasts for more than 10 ms (Figure 8h-i). The sensitivity analysis of τ_Ψ (Figure 8j) confirm that a localized BC does indeed increase the lifetime of the localization ($\tau_\Psi = [10 \sim 15]$ ms) and among the others the geometrical barrier due to the presence of a big spine apparatus plays a major role in causing longer localization of the second messenger.

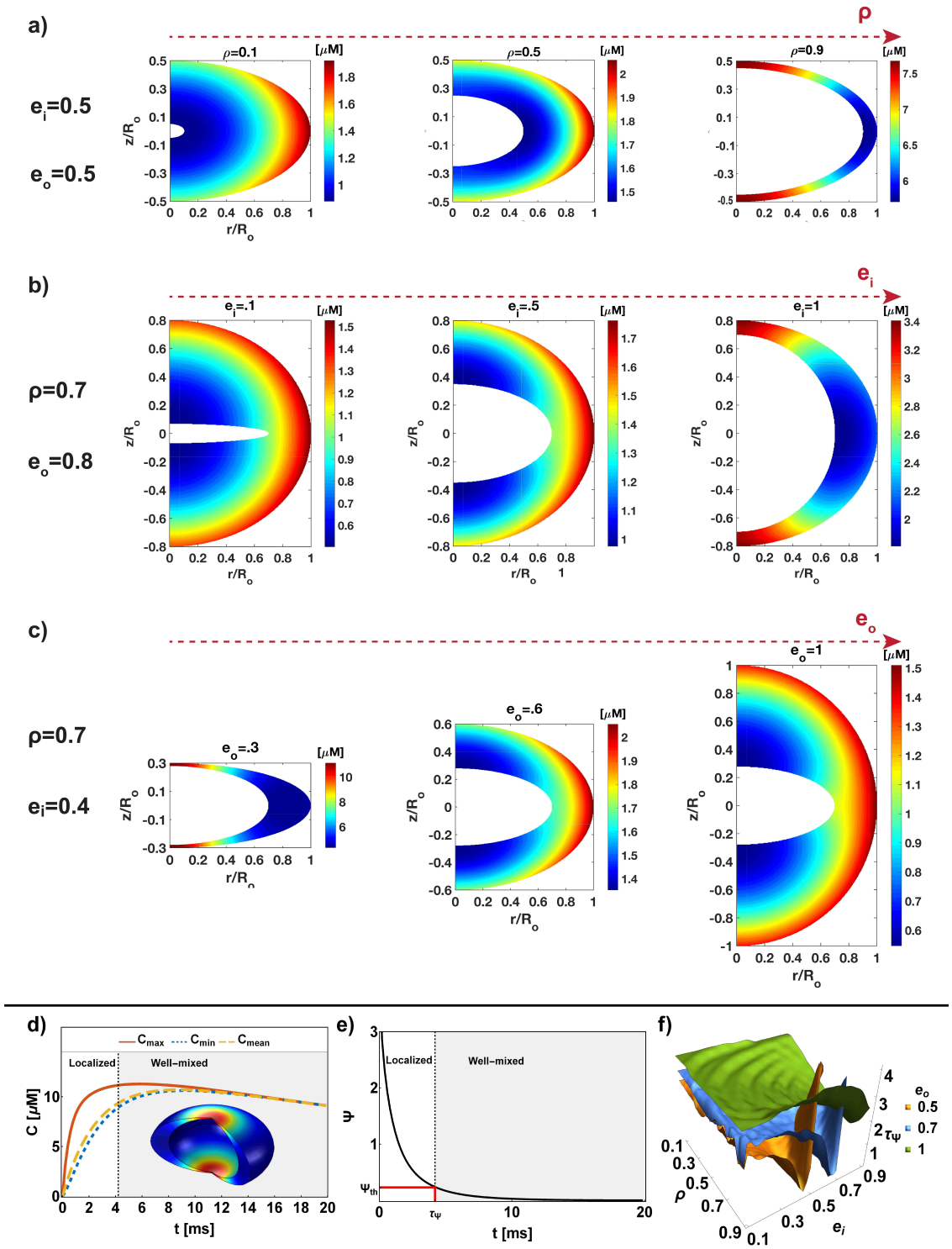

Figure 7: Effect of spine shape and spine apparatus shape on the spatial distribution of C. All simulations are shown for $D = 10\ \mu m^2/s$, $a_o = 250\ nm$ and $t = 1\ ms$: a) For $e_i = 0.5$ and $e_o = 0.5$, we analyzed the

(Figure 7 continued...)

Figure 7 (cont.): effect of increasing ρ. As ρ increases, the location of maximum concentration changes from the equator to the pole, and the maximum value increases as well. A similar behavior is highlighted in b) where the effect of the increase in internal eccentricity is shown, keeping fixed $\rho = 0.7$ and $e_o = 0.8$. In comparison, c) shows opposite behavior, when moving toward a more spheroidal outer shape ($e_o \to 1$), keeping fixed $\rho = 0.7$ and $e_i = 0.4$. The time evolution C_{max}, C_{min}, and C_{mean} is plotted in d) considering a spine with $\rho = 0.9$, $e_i = 0.5$, and $e_o = 0.5$ highlighting how a significant localizations holds for few ms before a well-mixed distribution is reached. The parameter Ψ is plotted in e) and we showed in f) smoothed surfaces τ_Ψ highlighting how the lifetime of the localization depends on the geometrical parameters.

3.5 Nonlinear reaction kinetics affects the spatiotemporal dynamics of C in the long timescale

Thus far, we have only considered linear kinetics of second messenger decay within the domain. However, signal transduction events are often nonlinear, particularly in the dendritic spine [31, 72, 73]. We extended our model to investigate whether nonlinear kinetics would change the effect of geometry and BCs. To do this, we modified the reaction-diffusion equation in Eq. (1) to include a Michaelis–Menten [74] kinetics as follows:

$$\frac{\partial C}{\partial t} + V_{max}\frac{C}{K_M + C} = D\nabla^2 C, \tag{34}$$

where the maximum rate is $V_{max} = C_{max}/\tau$ and K_M is the Michaelis-Menten constant.

We performed the simulations with $C_{max} = 6$ μM, $\tau = 50$ ms, and $K_M = 3$ μM and compared the results obtained with linear reaction kinetics (Eq. (1)). The comparison of all the case previously presented (Figure 9a-c) showed that the complexity introduced with a nonlinear reaction does not affect the spatiotemporal dynamics of second messenger in the short timescale ($t < 10$ ms), but affects the long-term dynamics showing a decay with different slopes. Furthermore, the localization and value of the maximum concentration does not depend on the kinetics, but rather is governed by the geometry and BCs. The kinetics affects the dynamics when a well-mixed distribution is already reached in all three cases, exhibiting different decay rates.

4 Discussion

Recent experimental observations have presented detailed, high-resolution images of the architecture of dendritic spines highlighting a complex internal organization [37, 68–71]. Such observations serve to highlight the role of geometry and spatial features in cellular phenomena. In this work, we used a general framework to study the effect of spine geometry including internal organization in an idealized mathematical model with the goal of identifying some governing principles that regulate the spatio-temporal dynamics of second messengers. To do this, we developed and analyzed a general mathematical model, in which, a reaction-diffusion partial differential equation (PDE) with time-dependent mixed boundary conditions (BCs) we analytically and numerically solved.

Numerical simulations demonstrated how the shape of the spine governs the transient localization of peak of concentration of second messengers. The lifetime of this localization depends nonlinearly on the morphology. Furthermore, we also showed that localized BCs, confined to a portion of the boundary, resulted in an overall increase in the timescale of second messenger localization. Analytical investigation (Section 3.1)

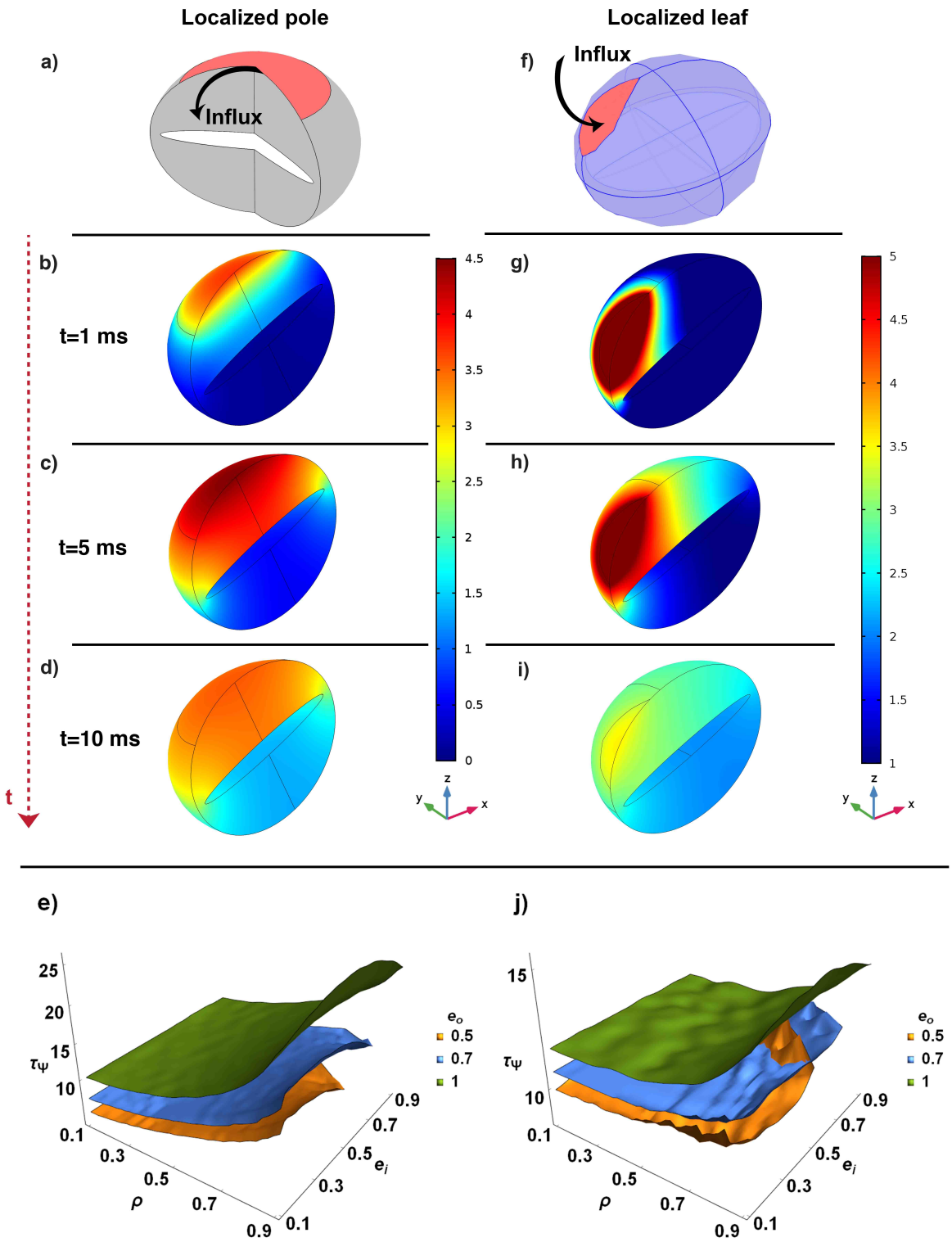

Figure 8: Effect of localized flux at the outer membrane of the spine. All the simulations shown

(Figure 8 continued...)

Figure 8 (cont.): use $D = 10\ \mu m^2/s$, $a_o = 250\ nm$. In the schematic a) and b) we analyzed the localized pole and leaf cases respectively considering the geometrical parameters $\rho = 0.9$, $e_o = 0.8$, and $e_i = 0.1$. We showed the distribution of C at $t = 1$ ms b) and g), $t = 5$ ms c) and h), and $t = 10$ ms d) and i). The τ_Ψ surfaces in e) and j) for $e_o = 0.5$, 0.7, and 1 show the nonlinear dependence of the lifetime of the localization to the geometrical parameters. The localized boundary condition increases the lifetime of the overall gradient, in particular, the geometrical barrier represented by a big ER ($\rho \to 0.9$) leads to a much more persistent localization in comparison to the uniformly distributed fluxes ($\tau_\Psi = [5 \sim 26]\ ms$).

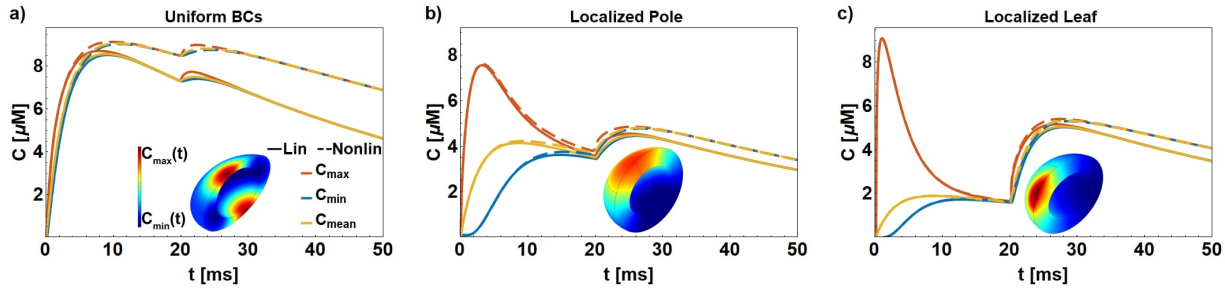

Figure 9: Comparison between linear (solid lines) and nonlinear (dashed lines) kinetics for the ellipsoidal geometry with uniform BCs a), localized pole b), and localized leaf c). The nonlinear nature of the kinetics does not change the localization of the maximum (in red), minimum (in blue), and the lifetime of the localization. However, the nonlinear kinetics affect the long timescale dynamics ($t > 10$ ms) when the minimum and maximum converge to the spatial average (yellow) resulting in a decay with a different slope.

showed that geometry dictates the specific kind of harmonic function of the spatial distribution of second messenger. The temporal dynamics in the long time is governed by the kinetics of signaling reaction in the cytoplasm. However, this separation of temporal and spatial effects is not straightforward. The time-dependent BCs (Eq. (2)) represent both the kinetics of the membrane reactions and the curvature of the boundary (in the $\nabla C \cdot \hat{\mathbf{n}}$ term). Therefore, time-dependent BCs represent the coupling between shape and kinetics (Figure 10).

Even though our model is simplified, it allows us to identify some common principles by which geometry can be used to alter timescales of signal transduction. The notion that shape alone can affect signal transduction (Figures 6 and 7) is a principle that is now being well-accepted in the literature [3–5, 7–10] and we now extend this idea to signaling subcompartments such as dendritic spines. Another emerging idea in shape regulation of signaling is the role played by organelles such as the endoplasmic reticulum and nucleus [47, 75]. In the case of spines, the spine apparatus is thought to play a critical role in governing synaptic plasticity [38–44]. We find that the relative organization of the two membranes, PM and the ER membrane, affect the geometric landscape through both shape and boundary condition effects. We also find that the organelles can act as a physical barrier to diffusion extending the lifetime of the gradient. And finally, at short timescales, the nature of the kinetics in the cytoplasm does not alter our conclusions but kinetics play an important role in the long timescale especially in coupled cascades [3, 5, 76, 77]. These predictions are applicable not just to spines but also to cells in general.

Despite the relatively simple model presented here, we found that the spatial dependence of second messenger at short timescales was nonintuitive and exhibited a complex dependence on geometry. Based on

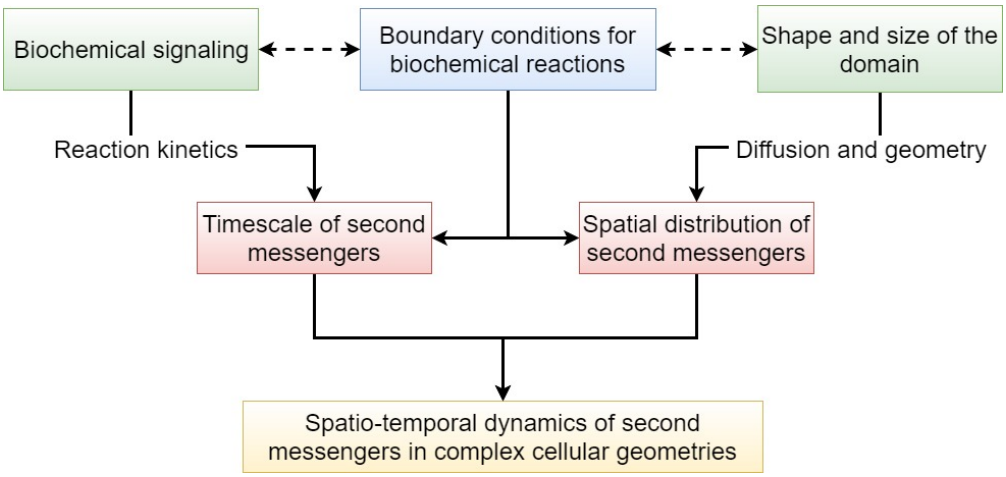

Figure 10: Geometric principles of second messenger dynamics: The spatio-temporal dynamics of second messenger are affected by the interplay of shape and size, biochemical signaling, and membrane reactions through boundary conditions. Our study showed that the amplitude of the harmonic functions found in the analytical solution and dictated by the geometry, intricately depend on the boundary condition in the short-timescale and on the reaction kinetics on long-timescale

these insights, the next steps in spine systems biology can focus on specific signal transduction pathways and use reconstructions of realistic geometries to identify how the simple mathematics presented here translate into computational biology. Additionally, experimentally advances in localized imaging of second messenger molecules will be necessary to test and validate the predictions made by computational modeling. These combined efforts will enable us to extend these simple models to biologically relevant processes.

Acknowledgments

We thank Dr. Lucas Stolerman and Ms. Miriam Bell, for the feedback on the manuscript. AC, TMB, TJS, and PR would also like to thank the AFOSR (grant number FA9550-18-1-0051) and RI the NIH (grant number GM072853) for funding support.

Conflict of interest

AC, TMB, TJS, RI, and PR declare that they have no conflict of interest.

Author Contributions

P.R. designed the study. A.C. developed the analyses and performed the simulations. All authors discussed the results, wrote the text and contributed to the final version of the manuscript.

Appendix A 30-fold slow down for the diffusion constant of second messengers in dendritic spines

It has been recently hypothesized that for the experimentally observed compartmentalized responses to occur, diffusion of second messengers, such as $cAMP$, in the cytoplasm must be much slower than the rate of free diffusion measured in dilute aqueous solutions. As a matter of fact, Agarwal *et al.* [63] measured diffusion rates from 4 to 30 fold slower than the rate of free diffusion ($D_{cAMP} = [5-76]\ \mu m^2/s$); decreases that Yang *et al.* [64] attributed to higher collision with the other macromolecules in the intracellular environment due to molecular crowding. Other parallel experimental studies have found that the effective diffusion of IP_3 is ~ 30 fold slower than the value reported by Allbritton *et al.* ($D_{IP_3} = 283\ \mu m^2/s$) [62], claiming that $D_{IP_3} = [3{-}10]\ \mu m^2/s$ [78]. Moreover, similar measurements were found for the diffusion of calcium ($D_{Ca^{2+}} = [13-65]\ \mu m^2/s$) at physiological concentrations, where the diffusion rate depends on the concentration of free calcium, and on the presence of mobile or immobile buffer binding sites [62]. In neurons, an upper bound for diffusion coefficient of $D_{Ca^{2+}} \simeq 16/, \mu m^2/s$ were detected by Gabso and Neher [65] conferring to fixed binding sites, eventually located on cell organelles or cytoskeletal elements, the retarding role. In dendritic spines, a ~ 20 fold reduction in calcium diffusion rate with respect to calcium's free diffusion rate in water was experimentally measured and simulated in silico by Biess *et al.* [66] ($D_{Ca^{2+}} \simeq 30\,\mu m^2/s$). It is well-known that dendritic spines are more viscous and rich in actin filaments than other cells, and all these experimental values seem to be consistent with theoretical estimates for the diffusion of particles inside polymeric gels. Indeed, following Cai *et al.* [67] the diffusivity of particles smaller than the average distance from a monomer on one chain to the nearest monomer on another chain (the so-called *correlation length*) can be estimated by the following relationship:

$$D = k_B T/(\eta_s d), \tag{A.1}$$

where k_B is the Boltzmann constant, T the absolute temperature, η_s the solvent viscosity, and d the particle diameter. Specializing the previous relationship for calcium ions ($d_{Ca^{2+}} \simeq\ 200\ pm$) in dendritic spines characterized by an uniquely large viscosity, from 4 to 5 times higher than the other cell types, consistent with a high density of solubilized proteins ($\eta_s = 19.9/(2\pi)\ Pa \cdot s$ [79]) the estimate in Eq. (A.1) for the diffusion constant of calcium in spine at physiological conditions ($T = 310\ K$) is

$$D_{Ca^{2+}} \simeq 7\mu m^2/s.$$

showing that, theoretically also, in dendritic spines there is a drastic reduction diffusivity of molecules, with respect the free diffusion in water.

Appendix B Non-smoothened τ_Ψ surface plots

In the main text, we presented smoothed τ_Ψ surfaces for the case of spatially uniformly distributed flux Figure 7f, localized influx in the pole of the spine Figure 8e, and in the side of the spine Figure 8j. The surfaces were produced performing a low-pass filtering with a cut off frequency of $\omega = 1.5$ of the raw data from the simulations (Figures B.1–B.3).

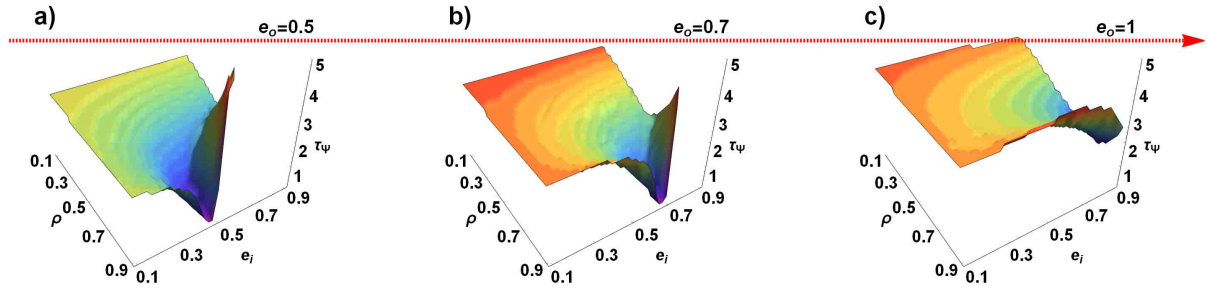

Figure B.1: Unfiltered version of surface plots τ_Ψ for uniformly distributed flux case in Figure 7f). All the simulations shown, use $D = 10\ \mu m^2/s,\ a_o = 250\ nm$. We created the plot using a regular mesh grid of 1681 points in the plane $\rho \times e_i$ both in the range $[0.1, 0.9]$. Due to the complexity of the phase field, for sake of clarity we considered, three different outer eccentricities separately: $e_o = 0.5$ a), $e_o = 0.7$ b), and $e_o = 1$ c).

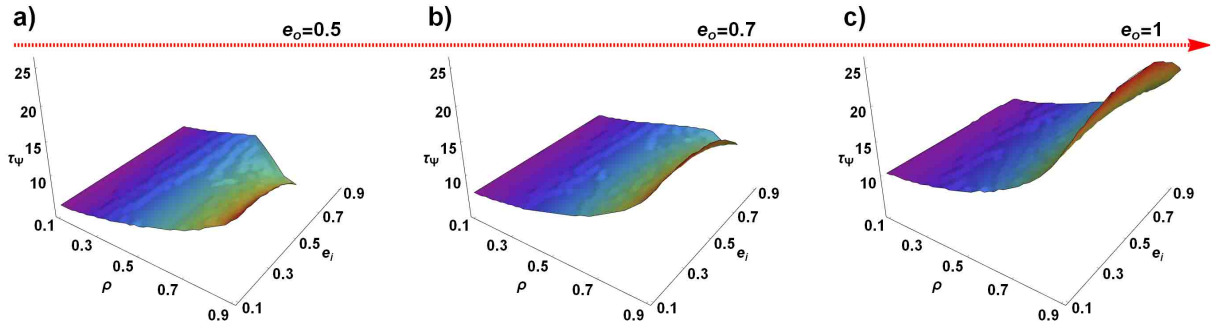

Figure B.2: Unfiltered version of surface plots τ_Ψ for localized plot case in Figure 8e. All the simulations shown, use $D = 10\ \mu m^2/s,\ a_o = 250\ nm$. We created the plot using a regular mesh grid of 1681 points in the plane $\rho \times e_i$ both in the range $[0.1, 0.9]$. Due to the complexity of the phase field, for sake of clarity we considered, three different outer eccentricities separately: $e_o = 0.5$ a), $e_o = 0.7$ b), and $e_o = 1$ c).

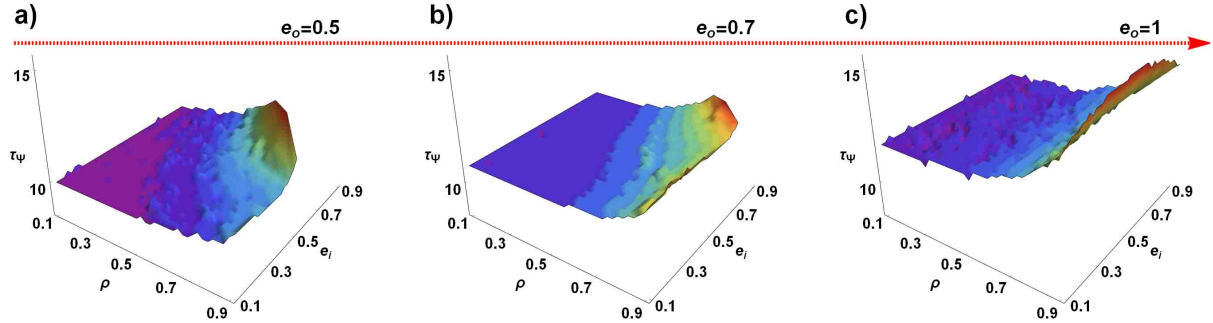

Figure B.3: Unfiltered version of surface plots τ_Ψ for localized leaf case in Figure 8j. All the simulations shown, use $D = 10\ \mu m^2/s,\ a_o = 250\ nm$. We created the plot using a regular mesh grid of 1681 points in the plane $\rho \times e_i$ both in the range $[0.1, 0.9]$. Due to the complexity of the phase field, for sake of clarity we considered, three different outer eccentricities separately: $e_o = 0.5$ a), $e_o = 0.7$ b), and $e_o = 1$ c).

References

1. Zaccolo, M. *et al.* Discrete Microdomains with High Concentration of cAMP in Stimulated Rat Neonatal Cardiac Myocytes. *Science* **295,** 1711–1715 (2002).
2. Brown, G. C. *et al.* Spatial gradients of cellular phospho-proteins. *FEBS Lett.* **457,** 452–454 (1999).
3. Kholodenko, B. N. *et al.* Signalling ballet in space and time. *Nat. Rev. Mol. Cell Biol.* **11,** 414–426 (2010).
4. Meyers, J. *et al.* Potential for Control of Signaling Pathways via Cell Size and Shape. *Curr. Biol.* **16,** 1685–1693 (2006).
5. Kholodenko, B. N. Cell-signalling dynamics in time and space. *Nat. Rev. Mol. Cell Biol.* **7,** 165–176 (2006).
6. Bartol, T. M. *et al.* Computational reconstitution of spine calcium transients from individual proteins. *Front. Synaptic Neurosci.* **7,** 1–24 (2015).
7. Rangamani, P. *et al.* Decoding information in cell shape. *Cell* **154,** 1356–69 (2013).
8. Thalmeier, D. *et al.* Geometry-induced protein pattern formation. *Proc. Natl. Acad. Sci.* **113,** 548–553 (2016).
9. Craske, M. L. *et al.* Spines and neurite branches function as geometric attractors that enhance protein kinase C action. *J Cell Biol.* **170,** 1147–1158 (2005).
10. Onsum, M. D. *et al.* Morphology matters in immune cell chemotaxis: membrane asymmetry affects amplification. *Phys. Biol.* **3,** 190–199 (2006).
11. Bao, M. *et al.* 3D microniches reveal the importance of cell size and shape. *Nat. Commun.* **8,** 1962 (2017).
12. Bloodgood, B. L. *et al.* Ca2+ signaling in dendritic spines. *Curr. Opin. Neurobio.* **17,** 345–351 (2007).
13. Higley, M. J. *et al.* Calcium signaling in dendrites and spines: practical and functional considerations. *Neuron* **59,** 902–13 (2008).
14. Sabatini, B. L. *et al.* Ca2+ signaling in dendritic spines. *Curr. Opin. Neurobio.* **11,** 349–356 (2001).
15. Cajal, S. Estructura de los centros nerviosos de las aves. *Rev. Trim. Histol. Norm. Pat.* 1–10 (1888).
16. Golgi, C. Sulla Struttura Della Sostanza Grigia Del Cervello(Comunicazione Preventiva). *Gazz. Med. Ital.* 244–246 (1873).
17. Gray, E. G. Electron microscopy of synaptic contacts on dendrite spines of the cerebral cortex. *Nature.* eprint: `13829103` (1959).
18. Yasuda, R. Biophysics of Biochemical Signaling in Dendritic Spines: Implications in Synaptic Plasticity. *Bioph. J.* **113,** 2152–2159 (2017).
19. Kotaleski, J. H. *et al.* Modelling the molecular mechanisms of synaptic plasticity using systems biology approaches. *Nat. Rev. Neurosci.* **11,** 239–251 (2010).
20. Bourne, J. N. *et al.* Balancing Structure and Function at Hippocampal Dendritic Spines. *Ann. Rev. Neurosci.* **31,** 47–67 (2008).
21. Nishiyama, J. *et al.* Biochemical Computation for Spine Structural Plasticity. *Neuron* **87,** 63–75 (2015).
22. Noguchi, J. *et al.* State-dependent diffusion of actin-depolymerizing factor/cofilin underlies the enlargement and shrinkage of dendritic spines. *Sci. Rep.* **6,** 32897 (2016).

23. Bernardinelli, Y. *et al.* Structural plasticity: mechanisms and contribution to developmental psychiatric disorders. *Front. Neuroanat.* **8,** 123 (2014).

24. Heck, N. *et al.* Editorial: Dendritic spines: from shape to function. *Front. Neuroanat. Frontiers Research Topics* **9** (eds Heck, N. *et al.*) (2015).

25. Spiga, S. *et al.* The addicted spine. *Front. Neuroanat.* **8,** 110 (2014).

26. Oertner, T. G. *et al.* Calcium regulation of actin dynamics in dendritic spines. *Cell Calcium* **37,** 477–482 (2005).

27. Lai, K.-O. *et al.* Structural plasticity of dendritic spines: The underlying mechanisms and its dysregulation in brain disorders. *Bioch. et Biophy. Acta (BBA) - Mol. Basis of Dis.* **1832,** 2257–2263 (2013).

28. Gipson, C. D. *et al.* Structural and functional plasticity of dendritic spines - root or result of behavior? *Genes, Brain and Behav.* **16,** 101–117 (2017).

29. Sorra, K. E. *et al.* Overview on the structure, composition, function, development, and plasticity of hippocampal dendritic spines. *Hippocampus* **10,** 501–11 (2000).

30. Mohapatra, N. *et al.* Spines slow down dendritic chloride diffusion and affect short-term ionic plasticity of GABAergic inhibition. *Sci. Rep.* **6,** 23196 (2016).

31. Ramirez, S. A. *et al.* Dendritic spine geometry can localize GTPase signaling in neurons. *Mol.r Biol. Cell* **26** (ed Edelstein-Keshet, L.) 4171–4181 (2015).

32. Higley, M. J. *et al.* Calcium Signaling in Dendritic Spines. *Cold Spring Harb. Perspect. Biol.* **4,** 1–18 (2012).

33. Byrne, M. J. *et al.* The impacts of geometry and binding on CaMKII diffusion and retention in dendritic spines. *J. Comput. Neurosci.* **31,** 1–12 (2011).

34. Holcman, D. *et al.* Calcium dynamics in dendritic spines and spine motility. *Bioph. J.* **87,** 81–91 (2004).

35. Cooney, J. R. *et al.* Endosomal Compartments Serve Multiple Hippocampal Dendritic Spines from a Widespread Rather Than a Local Store of Recycling Membrane. *J. Neurosci.* **22,** 2215–2224 (2002).

36. Spacek, J. *et al.* Three-Dimensional Organization of Smooth Endoplasmic Reticulum in Hippocampal CA1 Dendrites and Dendritic Spines of the Immature and Mature Rat. *J. Neurosci.* **17,** 190–203 (1997).

37. Wu, Y. *et al.* Contacts between the endoplasmic reticulum and other membranes in neurons. *Proc. Natl. Acad. Sci.* **114,** 4859–4867 (2017).

38. Jedlicka, P. *et al.* A role for the spine apparatus in LTP and spatial learning. *Behav. Brain Res.* **192,** 12–19 (2008).

39. Deller, T. *et al.* Synaptopodin-deficient mice lack a spine apparatus and show deficits in synaptic plasticity. *Proc. Natl. Acad. Sci.* **100,** 10494–10499 (2003).

40. Frotscher, M. *et al.* Fine structure of synapses on dendritic spines. *Front. Neuroanat.* **8** (2014).

41. Segal, M. *et al.* Endoplasmic reticulum calcium stores in dendritic spines. *Front. Neuroanat.* (2014).

42. Korkotian, E. *et al.* Synaptopodin Regulates Spine Plasticity: Mediation by Calcium Stores. *J. Neurosci.* **34,** 11641–11651 (2014).

43. Webb, D. *et al.* Dendritic spine morphology and dynamics in health and disease. *Cell Health and Cytoskelet.* 121 (2015).

44. Adrian, M. *et al.* Barriers in the brain: resolving dendritic spine morphology and compartmentalization. *Front. Neuroanat* **8,** 1–12 (2014).

45. Jedlicka, P. *et al.* Understanding the role of synaptopodin and the spine apparatus in Hebbian synaptic plasticity. New perspectives and the need for computational modeling. *Neurobiol. Learn. Mem.* **138,** 21–30 (2017).

46. Ngo-Anh, T. J. *et al.* SK channels and NMDA receptors form a Ca2+-mediated feedback loop in dendritic spines. *Nat. Neurosci.* **8,** 642–649 (2005).

47. Calizo, R. C. *et al.* Curvature regulates subcellular organelle location to control intracellular signal propagation. *bioRxiv,* 1–47 (2017).

48. Jahr, C. E. *et al.* Calcium permeability of the N-methyl-D-aspartate receptor channel in hippocampal neurons in culture. *Proc. Natl. Acad. Sci.* **90,** 11573–11577 (1993).

49. Shouval, H. Z. *et al.* A unified model of NMDA receptor-dependent bidirectional synaptic plasticity. *Proc. Natl. Acad. Sci.* **99,** 10831–10836 (2002).

50. Rackham. A Ca2+-based computational model for NDMA receptor-dependent synaptic plasticity at individual post-synaptic spines in the hippocampus. *Front. Synaptic Neurosci.* **2,** 31 (2010).

51. Wolfram Research Inc. *Mathematica v. 11.3* Champaign, Illinois, 2018.

52. COMSOL Inc. Introduction to COMSOL Multiphysics, version 5.3a. *COMSOL Man.* **5.3a,** 196 (2017).

53. The MathWorks Inc. *MATLAB 2018a* Natick, Massachusetts, 2018.

54. Haberman, R. *Applied Partial Differential Equations with Fourier Series and Boundary Value Problems, Books a la Carte* 5th, 756 (Pearson, 2012).

55. Arscott, F. M. *et al.* Curvilinear Co-ordinate Systems in which the Helmholtz Equation Separates. *IMA J. Appl. Math.* **27,** 33–70 (1981).

56. Arscott, F. M. *Periodic differential equations: an introduction to Mathieu, Lamé, and allied functions* (Pergamon, 1964).

57. Weisstein, E. W. Prolate Spheroidal Coordinates. *MathWorld - A Wolfr. Web Resour.*

58. Weisstein, E. W. Spherical Coordinates. *MathWorld- A Wolfr. Web Resour.*

59. Meixner, J. *et al. Mathieu Functions and Spheroidal Functions and their Mathematical Foundations* 130 (Springer-Verlag Berlin Heidelberg, 1980).

60. Xiao, H. *et al.* Prolate spheroidal wavefunctions, quadrature and interpolation. *Inverse Probl.* **17,** 805–838 (2001).

61. Müller, D. *et al.* Spheroidal eigenfunctions of the tidal equation. *Phys. Rev. Lett.* (1994).

62. Allbritton, N. *et al.* Range of messenger action of calcium ion and inositol 1,4,5-trisphosphate. *Science* **258,** 1812–1815 (1992).

63. Agarwal, S. R. *et al.* Mechanisms Restricting Diffusion of Intracellular cAMP. *Sci. Rep.* **6,** 1–11 (2016).

64. Yang, P. C. *et al.* A Computational Modeling and Simulation Approach to Investigate Mechanisms of Subcellular cAMP Compartmentation. *PLoS Comp. Biol.* **12,** 1–23 (2016).

65. Gabso, M. *et al.* Low mobility of the Ca2+ buffers in axons of cultured Aplysia neurons. *Neuron* **18,** 473–481 (1997).

66. Biess, A. *et al.* Barriers to Diffusion in Dendrites and Estimation of Calcium Spread Following Synaptic Inputs. *PLoS Comp. Biol.* **7** (ed Crampin, E. J.) 1002182 (2011).

67. Cai, L. H. *et al.* Mobility of nonsticky nanoparticles in polymer liquids. *Macromolecules* **44,** 7853–7863 (2011).

68. Capani, F. *et al.* Selective localization of high concentrations of F-actin in subpopulations of dendritic spines in rat central nervous system: A three-dimensional electron microscopic study. *J.Comp. Neurol.* **435,** 156–170 (2001).

69. Basu, S. *et al.* Quantitative 3-D morphometric analysis of individual dendritic spines. *Sci. Rep.* **8,** 1–13 (2018).

70. Toni, N. *et al.* Synapse formation on neurons born in the adult hippocampus. *Nat. Neurosci.* **10,** 727–734 (2007).

71. Shoop, R. D. *et al.* Ultrastructure of a Somatic Spine Mat for Nicotinic Signaling in Neurons. *J. Neurosci.* **22,** 748–756 (2002).

72. Rangamani, P. *et al.* Paradoxical signaling regulates structural plasticity in dendritic spines. *Proc. Natl. Acad. Sci.* **113,** 5298–5307 (2016).

73. Pi, H. J. *et al.* Coupled Phosphatase and Kinase Switches Produce the Tristability Required for Long-Term Potentiation and Long-Term Depression. *J. Neurosci.* **28,** 13132–13138 (2008).

74. Johnson, K. A. *et al.* The Original Michaelis Constant: Translation of the 1913 Michaelis-Menten Paper. *Biochemistry* **50,** 8264–8269 (2011).

75. Jain, N. *et al.* Cell geometric constraints induce modular gene-expression patterns via redistribution of HDAC3 regulated by actomyosin contractility. *Proc. Natl. Acad. Sci.* **110,** 11349–11354 (2013).

76. Bhalla, U. S. *et al.* Emergent properties of networks of biological signaling pathways. *Science* **283,** 381–7 (1999).

77. Bhalla, U. S. Synaptic input sequence discrimination on behavioral timescales mediated by reaction-diffusion chemistry in dendrites. *ELife* **6** (2017).

78. Dickinson, G. D. *et al.* Hindered cytoplasmic diffusion of inositol trisphosphate restricts its cellular range of action. *Science Signaling* **9,** 1–10 (2016).

79. Smith, B. A. *et al.* Dendritic spine viscoelasticity and soft-glassy nature: Balancing dynamic remodeling with structural stability. *Bioph. J.* **92,** 1419–1430 (2007).